Quantitative excited state spectroscopy of a single InGaAs quantum dot molecule through multi-million-atom electronic structure calculations

Muhammad Usman[1,5,6], Yui-Hong Matthias Tan[1,6], Hoon Ryu[1], Shaikh S Ahmed[2], Hubert J Krenner[3], Timothy B Boykin[4] and Gerhard Klimeck[1]

[1] School of Electrical and Computer Engineering and Network for Computational Nanotechnology, Purdue University, West Lafayette, IN 47906, USA
[2] Department of Electrical and Computer Engineering, Southern Illinois University at Carbondale, Carbondale, IL 62901, USA
[3] Lehrstuhl für Experimentalphysik 1, Universität Augsburg, Universitätsstraße 1, D-86159 Augsburg, Germany
[4] Department of Electrical and Computer Engineering, University of Alabama in Huntsville, Huntsville, AL 35899, USA

E-mail: usman@alumni.purdue.edu

Abstract

Atomistic electronic structure calculations are performed to study the coherent inter-dot couplings of the electronic states in a single InGaAs quantum dot molecule. The experimentally observed excitonic spectrum by Krenner *et al* (2005) *Phys. Rev. Lett.* **94** 057402 is quantitatively reproduced, and the correct energy states are identified based on a previously validated atomistic tight binding model. The extended devices are represented explicitly in space with 15-million-atom structures. An excited state spectroscopy technique is applied where the externally applied electric field is swept to probe the ladder of the electronic energy levels (electron or hole) of one quantum dot through anti-crossings with the energy levels of the other quantum dot in a two-quantum-dot molecule. This technique can be used to estimate the spatial electron–hole spacing inside the quantum dot molecule as well as to reverse engineer quantum dot geometry parameters such as the quantum dot separation.

Crystal-deformation-induced piezoelectric effects have been discussed in the literature as minor perturbations lifting degeneracies of the electron excited (P and D) states, thus affecting polarization alignment of wavefunction lobes for III–V heterostructures such as single InAs/GaAs quantum dots. In contrast, this work demonstrates the crucial importance of piezoelectricity to resolve the symmetries and energies of the excited states through matching the experimentally measured spectrum in an InGaAs quantum dot molecule under the influence of an electric field. Both linear and quadratic piezoelectric effects are studied for the first time for a quantum dot molecule and demonstrated to be indeed important. The net piezoelectric contribution is found to be critical in determining the correct energy spectrum, which is in contrast to recent studies reporting vanishing net piezoelectric contributions.

(Some figures in this article are in colour only in the electronic version)

[5] Present address: Tyndall National Institute, Lee Maltings, Dyke Parade, Cork, Ireland.
[6] Co-first authors, contributed equally.

1. Introduction and problem background

Quantum dots grown by strain-driven self-assembly attract a great deal of interest because they can be used to implement optical communication and quantum information processing [1, 2]. Recently, significant advancements in providing good stability, high experimental repeatability, electroluminescence and controlled coupling have made III–V quantum dots a potential candidate for quantum computers. Based on single qubit (quantum bit) realization with an exciton in a single quantum dot [3], optical quantum gates have also been obtained with both an exciton and a biexciton within one dot [4]. Coupled quantum dot molecules (QDMs), therefore, are good candidates for spin-based [5], charge-based [6] and exciton-based [7, 8] qubits. It is desirable to excite single excitons with external electric fields. Vertically stacked QDMs have been suggested to host single or double qubits; these can then be controlled by optical pulses, electrical fields or magnetic fields [7–11]. However, a very basic requirement necessary for realizing qubits in these structures is the prior achievement of entangled states between the two dots. In a recent experimental study [12], coherent quantum coupling in QDMs has been observed with different separation distances between two dots forming a QDM under the applied bias. However, a detailed quantitative study for the identification of the states in the spectrum and their coupling under linear and quadratic piezoelectric effects has been missing. The theoretical study accompanied with the experiment [12] is based on a single-band effective-mass model and considered only two lowest conduction band (E_1 and E_2) energy levels and two highest valence band (H_1 and H_2) energy levels. Thus figure 3(b) in the [12] plots only one anti-crossing ($E_1 \leftrightarrow H_1$) and compares it to the experimental measurement. Moreover, it did not take into account the effects of the nonlinear piezoelectricity because the nonlinear piezoelectric field polarization constants [24] were not available at the time of this study in 2005. Thus the published study did not include the symmetries of individual quantum dots nor did it model the energy state couplings quantitatively. In a quantum dot molecule, each quantum dot possesses a ladder of electronic energy levels which give rise to multiple anti-crossings due to the electric-field-induced Stark shift. It is therefore essential that more than two electron and hole energy levels should be considered to identify the correct energy states in the experimental measurements.

In this work, we present an atomistic theoretical analysis of the experimental measurement including alloy randomness, interface roughness, atomistic strain and piezoelectric-induced polarization anisotropy, and realistic sized boundary conditions, which we believe is essential to fully understand the complex physics of these multi-million-atom nanostructures [16]. Both linear and nonlinear components of the piezoelectric field are included. The net piezoelectric field is found to be critical to resolve the symmetries and energies of the excited states. Our theoretical optical transition strengths match with the experimental quantum dot state coupling strengths. Furthermore, we sweep the externally applied electrical field from 0 to 21 kV cm^{-1} to probe the symmetry of the electron states in the lower quantum dot based on the inter-dot energy level anti-crossings between the lower and the upper quantum dots. Such 'level anti-crossing spectroscopic' (LACS) analysis [37] can be used for a direct and precise measurement of energy levels of one quantum dot placed near another quantum dot in the direction of the applied electrical field. It can also be helpful to quantitatively analyze 'tunnel coupling energies' of the electron and hole energy states through the inter-dot energy level resonances in the single quantum dot molecule configuration predicted for the 'quantum information technologies' [12]. Finally the spacing between the anti-crossings and electric-field-induced Stark shifts allow us to 'reverse engineer' the separation between the quantum dots inside the quantum dot molecule.

Quantum dot molecules grown by self-assembly are mechanically coupled to each other through long-range strain originating from lattice mismatch between the quantum dot and the surrounding buffer. Despite the symmetric shape of the quantum dots (dome or lens shape), the atomistic strain is, in general, inhomogeneous and anisotropic, involving not only hydrostatic and biaxial components but also non-vanishing shear components [16, 26, 27]. Due to the underlying crystal symmetry theoretical modeling of these quantum dot molecules requires realistically spatially large extended boundary conditions to capture the correct impact of long-range strain on the electronic spectrum typically extending 30 nm into the substrate and 20 nm on both sides in the lateral direction. A detailed analysis of strain-induced coupling and shifts in band edges of identical and non-identical quantum dots has been presented in earlier publications [22, 36, 38].

2. Past studies of piezoelectric effects

III–V heterostructures such as InGaAs/GaAs quantum dots show piezoelectric effects originating from diagonal and shear strain components. The asymmetric piezoelectric potentials are critical in determining the correct anisotropy of electron p-states [23–29]. Past studies of quantum dot molecules [43] to investigate the effect of strain and inter-dot separations on entanglement of electronic states does not include piezoelectric effects. Recent studies based on atomistic pseudopotentials suggest for single InAs quantum dots [24, 25] that linear and quadratic piezoelectric effects tend to cancel each other, thus leading to an insignificant net piezoelectric effect. Another study based on a $k \cdot p$ continuum method [30] used experimental polarization constants (see the first row in table 1) that overestimated the piezoelectric effect by 35–50% for coupled quantum dot systems [23]. This work, for the first time, based on realistically sized boundary conditions and a three-dimensional atomistic material representation, takes into account the correct atomistic asymmetry and built-in electrostatic fields. Linear and quadratic polarization constants (see table 1) recently calculated using *ab initio* calculations [23] are used to study the impact of piezoelectric effect on excitonic spectra. Our calculations on a QDM show a non-vanishing net piezoelectric effect which is critical in reproducing experimental excitonic spectra [12]. Such non-vanishing piezoelectric potentials in single quantum dots

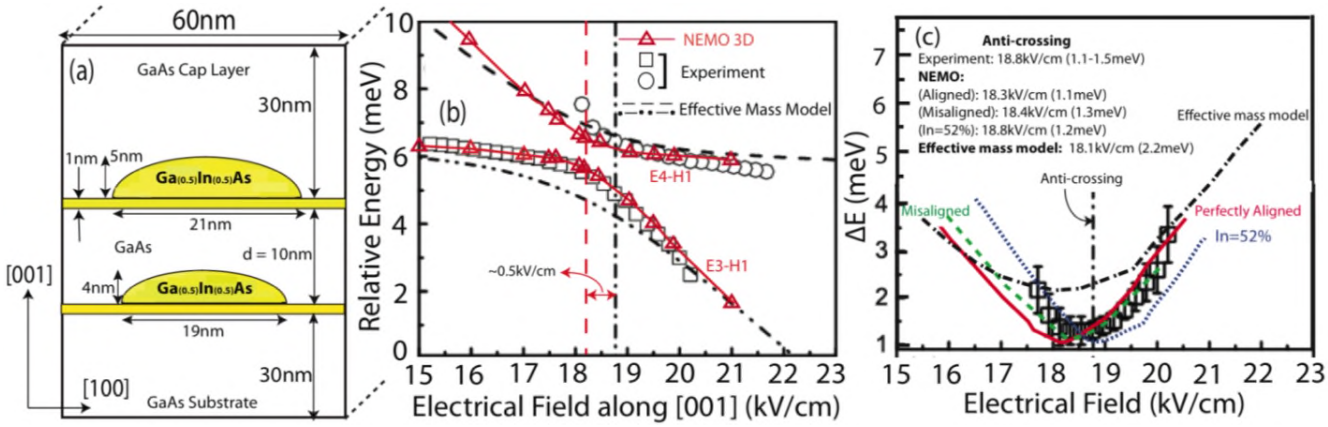

Figure 1. (a) Model system consisting of two lens-shaped $In_{0.5}Ga_{0.5}As$ quantum dots vertically stacked and separated by a 10 nm GaAs buffer as described in the experiment. Both quantum dots are placed on 1 nm thick $In_{0.5}Ga_{0.5}As$ wetting layers. Substrate and cap layer thicknesses are 30 nm. (b) NEMO 3D excitonic spectra (red triangles) for perfectly aligned quantum dots are compared with experimentally measurement (black circles and squares) [12] and effective mass calculation [12] (dotted lines) [12]. The NEMO 3D calculations match experiments quantitatively and give a much better estimate of tunnel coupling energy than the effective mass model [12]. (c) Difference energy of excitons (E_3, H_1) and (E_4, H_1) in (b) is compared for various cases. Black squares with error bars are from experimental data. Solid line (red) is from NEMO 3D structure in (a). Broken line (green) is for NEMO 3D where the upper quantum dot in (a) is shifted to the right by 0.5 nm. Dotted line (blue) is from NEMO 3D with $In_{0.52}Ga_{0.48}As$ quantum dots. Broken line with dots (black) is from the effective mass calculations [12]. A quantitative match of NEMO 3D with experiments is evident. Small variations in quantum dot location and alloy composition insignificantly change the electrical field of the anti-crossing and barely influence the exciton energy difference.

have also been predicted recently [26]. However, previous studies in the literature so far [23–30] describe piezoelectric effects as merely small perturbations that lift excited states (P- and D-states) degeneracies (increase their splitting) and/or flip the orientation of wavefunction lobes. This work is the first evidence that inclusion of the piezoelectric effect is indispensable to reproduce an experimentally observed excitonic spectrum in a quantum dot molecule system and to identify the correct energy states. Furthermore, optical transition intensities are calculated to characterize dark and bright excitons and matched with experimentally obtained transition strengths.

3. NEMO 3D simulator

In this paper, an experimentally observed optical spectrum [12] is reproduced and the excitonic states are identified using the Nano Electronic Modeling tool (NEMO 3D) [13–15]. NEMO 3D enables the atomistic simulation and computation of strain and electronic structure in multi-million-atom nanostructures. It can handle strain and electronic structure calculations consisting of more than 64 and 52 million atoms, corresponding to nanostructures of $(110\ \text{nm})^3$ and $(101\ \text{nm})^3$, respectively [14, 15]. Strain is calculated using an atomistic valence force field (VFF) method [18] with anharmonic corrections [31]. The electronic structure calculation is performed using a twenty-band $sp^3d^5s^*$ nearest-neighbor empirical tight binding model [17]. The tight binding parameters for InAs and GaAs have been published previously and are used without any adjustment [17]. The bulk-based atom-to-atom interactions are transferred into nanoscale devices where no significant bond charge redistribution or bond breaking is expected and strain is typically limited to around 8%. The strain and electronic structure properties of alloys are faithfully reproduced through an explicit disordered atomistic representation rather than an averaged potential representation. The explicit alloy representation also affords the ability to model device-to-device fluctuations, which are critical in today's devices. For realistic semiconducting nanoscale systems our tight binding approach, employed in NEMO 3D, has been validated quantitatively against experimental data in the past through the modeling of the Stark effect of single P impurities in Si [19], distinguishing P and As impurities in ultra-scaled FinFET devices [20], the valley splitting in miscut Si quantum wells on the SiGe substrate [21], sequences of InAs quantum dots in InGaAs quantum wells [16] and optical properties of single and bilayer quantum dots [44].

4. Simulated geometry

Figure 1(a) shows the simulated geometry, which consists of two vertically stacked lens-shaped $In_{0.5}Ga_{0.5}As$ quantum dots separated by a 10 nm GaAs buffer. As indicated in the experiment [12], the modeled upper quantum dot is larger in size (base = 21 nm, height = 5 nm) as compared to the lower quantum dot (base = 19 nm, height = 4 nm). In the lateral dimensions, the GaAs buffer size is set to 60 nm with periodic boundary conditions. The modeled GaAs substrate is 30 nm deep and the lattice constant is fixed at the bottom. A GaAs buffer with large lateral depth has been used to correctly capture the impact of long-range strain and piezoelectric effects which is critical in the study of such quantum dot devices [13, 14, 16, 26, 27]. The quantum dots are covered by another 30 nm GaAs capping layer where atoms are allowed to move at the top layer subject to an open boundary condition. The electronic structure calculation is

Table 1. Polarization constants for calculation of piezoelectric potential from [24]. The values for $In_{0.5}Ga_{0.5}As$ are obtained by linear interpolation between GaAs and InAs.

Polarization constant	Type of component	GaAs (C m^{-2})	InAs (C m^{-2})	$In_{0.5}Ga_{0.5}As$ (C m^{-2})
e_{14}	Linear (experiment)	−0.16	−0.045	−0.1025
e_{14}	Linear (calculated)	−0.23	−0.115	−0.1725
B_{114}	Quadratic (calculated)	−0.439	−0.531	−0.485
B_{124}	Quadratic (calculated)	−3.765	−4.076	−3.9205
B_{156}	Quadratic (calculated)	−0.492	−0.12	−0.306

conducted over a smaller domain embedded within the strain domain using closed boundary conditions. Since the electronic states of interest are closely confined inside the quantum dots a smaller electronic domain size is sufficient to model the confined electronic states. The strain domain comprises a volume of ∼15 million atoms and the electronic domain a volume of ∼9 million atoms. In accordance to the experiment, a static external electric field ($\vec{\mathbf{F}}$) is applied in the [001] growth direction and varied from 0 to 23 kV cm^{-1}.

We mention here that, based on the information provided by Krenner *et al* [12, 42][7] regarding Schottky contacts and varying doping profiles of the experimental QDM structure, we estimated built-in electric fields of ∼30 kV cm^{-1} using self-consistent Poisson–Schrödinger calculations. In accordance to the experiment, the applied electric field as shown in our figures is referred to the flat-band voltage. Thus, for an applied field of $\vec{\mathbf{F}} = 0$, the cumulative electric field including built-in fields in the quantum dot molecule is roughly zero (±0.5 kV cm^{-1}).

5. Match with experiment—experimental emission is from excited states

Figure 1(b) plots the excitonic energies as a function of applied bias. The curves indicated by circle and square data points are from experimentally obtained photoluminescence measurements [12]. The measurements identify two bright excitonic emissions forming a tunable, coherently coupled quantum system. The triangle data points are from NEMO 3D simulations. The excitonic spectra calculated here are based on a simple energy difference of the single-electron and-hole eigenenergies. The charge-to-charge interaction will reduce the optical gap by around 5 meV which we are ignoring in our calculations. We mention here that the experimental excitonic emission spectrum [12] was obtained through micro-photoluminescence experiments at low temperatures. An HeNe laser was used for excitation. In the experimental measurements, the excitation density (Pexc ∼ 2.5 W cm^{-2}) was kept low to ensure only generation of neutral single exciton species. We therefore conclude that the experimentally observed excitonic emissions solely stem from neutral excitons and therefore calculations based on single-electron and-hole eigenenergies are sufficient in understanding the experimental measurements.

Based on the simulation results, two excitons (E_3, H_1) and (E_4, H_1) are identified to match the experiment. Figure 1(c) compares the calculation of the exciton splitting $\Delta E = (E_4, H_1) - (E_3, H_1)$ obtained from NEMO 3D with the experiment and a single-band effective-mass calculation [12]. The splitting at the anti-crossing point ($\Delta E_{\min}$), referred to as the 'tunneling coupling energy' [12] or the 'anti-crossing energy' [37] is found to be ∼1.1 meV, which closely matches the experimental value of 1.1–1.5 meV. On the other hand, the effective mass model significantly overestimates the tunneling coupling energy, predicting a value of ∼2.2 meV. Quantum dot molecules grown by self-assembly processes are neither perfectly aligned vertically [34], nor can the 'In' fraction of the quantum dot material be precisely determined [35]. These parameters are subject to slight variations during self-organization of the quantum dot nanostructures. Theoretical studies using NEMO 3D on horizontally misaligned quantum dots (lateral misalignment = 0.5 nm) and slight variation in the 'In' fraction ($In_{0.52}Ga_{0.48}As$ quantum dots instead of $In_{0.5}Ga_{0.5}As$ quantum dots) show that these difficult-to-control experimental imperfections can shift anti-crossing points to slightly higher electric field values. For example, the anti-crossing point is found to be at 18.5 kV cm^{-1} for the misaligned quantum dots and at 18.7 kV cm^{-1} for increased indium fraction concentration as compared to 18.3 kV cm^{-1} for perfectly aligned $In_{0.5}Ga_{0.5}As$ quantum dots. The exciton tunnel coupling energies appear to be almost insensitive to such experimental variations. The theoretical values show a close quantitative match with the experimental value of 18.8 kV cm^{-1}, regardless of the small variations in quantum dot alignment and small alloy composition variations.

6. 'Schematic' band edge diagram—E_3–E_4 anti-crossing in the range of experimental field

Figure 2(a) shows the spatial distribution of the single-particle energy states in a 'schematic' band edge diagram with piezoelectric field effects at zero electric field. The wavefunction plots are inserted corresponding to each energy state to indicate their spatial occupation inside the quantum dot molecule and their single-atom or-molecule character. If the energy and position of H_1 are kept fixed and used as the center of the electrical field lever arm shift, the application of an external [001] electrical field will tilt the band edges such that the lower quantum dot energy levels will move down in energy. Since the center of the electrical field lever arm shift is set at the position of the upper quantum dot, the lower quantum dot energy levels will exhibit a strong shift in the energy whereas the upper quantum dot energy levels will experience only a small Stark shift. As the lower quantum dot energy levels are shifted down by the electrical field, they

[7] He provided us with details about the experimental set up through emails.

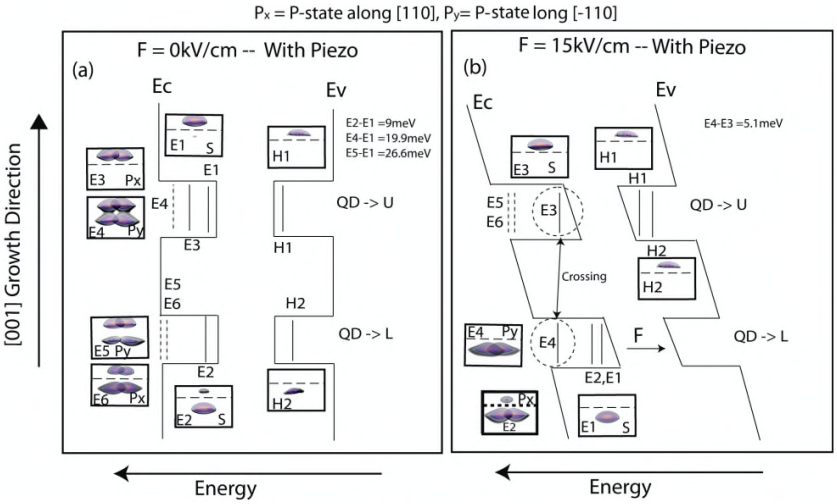

Figure 2. (a) Schematic lowest conduction (E_c) and highest valence band (E_v) edges with piezoelectric potential but zero external electric field. Wavefunction plots are inserted for each energy state as small insets. The dotted lines separate the upper and lower quantum dots. Ground hole and electron states reside in the upper quantum dot because of its larger size [22, 36, 38]. (b) Schematic lowest conduction (E_c) and highest valence band (E_v) edges with piezoelectric potential and with 15 kV cm^{-1} applied electric field. Wavefunction plots are inserted for each energy state as small insets. The dotted lines separate the upper and lower quantum dots. Arrows are marked to show the tilting of band edges and the directions of movement of energy states when the electric field is applied. The electric field pushes E_1 and E_2 to the lower quantum dot, causing excitons (E_1, H_1) and (E_2, H_1) to be optically inactive. At 15 kV cm^{-1}, E_3 makes a direct exciton with H_1 and hence will be optically active. Further increase in electric field strength beyond 15 kV cm^{-1} will push E_3 to the lower quantum dot and E_4 to the upper quantum dot resulting in an anti-crossing between E_3 with E_4 as observed in the experimental measurement [12].

anti-cross with the energy levels of the upper quantum dot and hence give rise to resonances. Figure 2(b) shows the new distribution of the energy levels at the electric field strength of 15 kV cm^{-1}. At 15 kV cm^{-1} it is quite evident that the lowest two-electron states (E_1 and E_2) have already moved into the lower quantum dot. The excited electron state E_3 located in the upper quantum dots creates a direct exciton (E_3, H_1) with H_1. The excited state E_4, is in the lower quantum dot and forms an indirect exciton (E_4, H_1) at $\vec{\mathbf{F}} = 15$ kV cm^{-1}. It can be anticipated that, with a further increase in the electric field >15 kV cm^{-1}, the conduction band edge will be tilted further. This will result in a decrease in the energy of E_4. The energy state E_3 will, therefore, anti-cross with the energy state E_4. This turns 'off' the optically active exciton (E_3, H_1) and turns 'on' the optically inactive exciton (E_4, H_1) as observed in the experiment [12]. Our calculations shown in figure 1(b) demonstrate the anti-crossing between the excitons (E_3, H_1) and (E_4, H_1) in the range of applied bias (15–23 kV cm^{-1}). A comprehensive spectroscopy of the energy levels for the electric fields spanning the 0–21 kV cm^{-1} range is presented in figure 3.

7. Electronic spectrum spectroscopy—H_1 is taken as reference

Figures 3(a) and (b) plot the electric field dependence of the lowest four conduction band energy levels (electron energy states E_1, E_2, E_3 and E_4) and the highest four valence band energy levels (hole energy states H_1, H_2, H_3 and H_4) for the experimental quantum dot molecular geometry under study with (a) and without (b) piezoelectric fields. The [001] electric field magnitude is varied from 0–21 kV cm^{-1}. The topmost valence band (hole ground) state H_1 resides in the upper quantum dot at zero applied electrical field due to the larger size of the upper quantum dot and the dominance of the heavy hole (HH) band under these strain conditions [22, 36, 38]. The reference for the electrical field shift 'lever arm' is set to the topmost valence band energy level H_1 to keep it fixed at its zero electrical field value. All the other energy levels are referenced to H_1.

8. Spectroscopy of conduction band states—three anti-crossings

As shown in figure 3(a), at the electric field $\vec{\mathbf{F}} = 0$, the ground electron state E_1 is in the upper quantum dot due to its larger size [22, 36]. E_2 is in the lower quantum dot, whereas E_3 and E_4 are in the upper quantum dot and show P_x, P_y-like symmetry. The same position and character of the electronic states at $\vec{\mathbf{F}} = 0$ are also shown in figure 2(a) using a schematic band edge diagram. The wavefunction plots are inserted corresponding to each energy state to indicate their spatial occupation inside the quantum dot molecule and their single-atom or-molecule character. As described earlier, the application of the external electric field tilts the conduction bands, pushing the lower quantum dot states to the lower energies (see also figure 2(b)). On their way down to lower energies, the lower quantum dot electron energy states anti-cross with the upper quantum dot electron energy states and exhibit molecular-like character. An anti-crossing results from the resonance of one quantum dot energy states (electron or hole) with the other quantum dot energy states when an external electric field is applied. At the resonance, the electron states become spatially delocalized over the two quantum dots

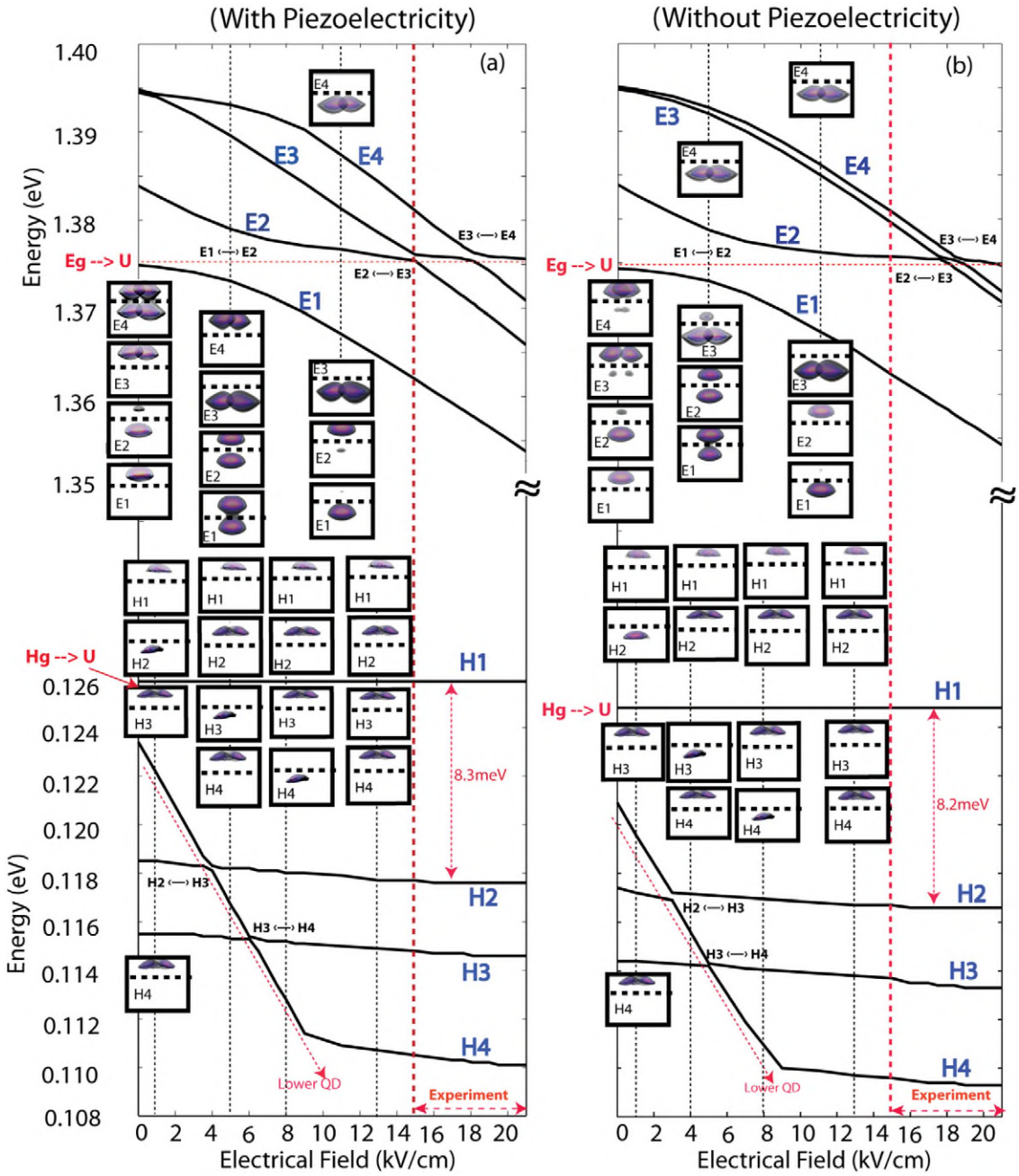

Figure 3. (a) and (b) Plot of first four electron and hole energy levels as a function of applied [001] electric field. The electric field is varied from 0 to 21 kV cm^{-1}. The H_1 energy is taken as the center of the electrical field lever arm so that its energy remains fixed at its zero electrical field value. Wavefunctions are inserted as small insets at critical values of the electric field to highlight the spatial position of the energy states inside the quantum dot molecule. The dotted lines in the wavefunction insets are marked to guide the eyes and separate the upper and lower quantum dots. Both the electron and the hole energy levels of the lower quantum dot exhibit anti-crossings with the energy levels of the upper quantum dot. The sequence of anti-crossings reveals the electron and hole level structure of the lower quantum dot and provide a direct measurement of the energy states in the lower quantum dot. The regions of the experimental electric fields (from 15 to 21 kV cm^{-1}) are zoomed-in in (c) and (d). (c), (d) Excitons (E_2, H_1), (E_3, H_1) and (E_4, H_1) are shown as a function of [001] electric field with (c) and without (d) piezoelectric effects. Insets show the wavefunction plots at (c) 15, 18.2 and 19.5 kV cm^{-1}, (d) 15, 18 and 19 kV cm^{-1}. The dotted lines in the wavefunction insets are marked to guide the eyes and separate the upper and lower quantum dots. In the case of no piezoelectricity, two anti-crossings clearly mismatch the experimental measurement [12]. (e), (f) Plots of the relative intensity of the interband optical absorption strengths as a function of the electric field with (e) and without (f) the piezoelectricity. The solid lines are from NEMO 3D calculations. Circles and triangles are from the experimental measurements [12]. It is clearly evident from the comparison of (e) and (f) that the piezoelectricity is critical to reproduce the experimentally measured optical spectra [12].

and form bonding- and anti-bonding-like molecular states. The hole states remain primarily localized in the separate dots. The separation between the anti-crossings provides a direct measurement of the energy levels of the lower quantum dot and hence enable 'reverse engineering' to determine the quantum dot dimension and symmetry. Such spectroscopic probing

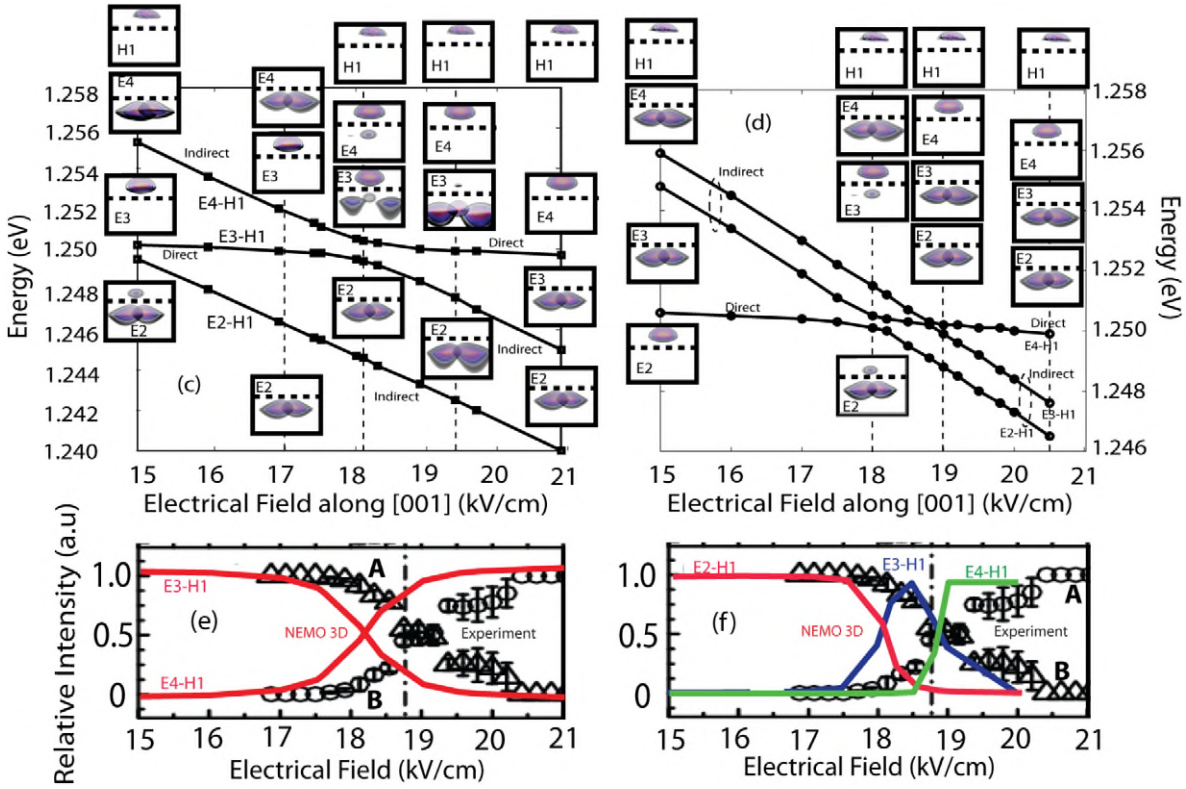

Figure 3. (Continued.)

of the hole energy states in a quantum dot molecule has been done recently [37] and referred to as 'level anti-crossing spectroscopy'.

Figure 3(a) shows the distribution of three anti-crossings ($E_1 \leftrightarrow E_2$, $E_2 \leftrightarrow E_3$ and $E_3 \leftrightarrow E_4$) between the electron energy levels. At $\vec{F} = 0$, E_1 is the upper quantum dot and E_2 is the lower quantum dot. The first anti-crossing $E_1 \leftrightarrow E_2$ results from the resonance of two s-type electronic states E_1 and E_2 when the electrical field is in the range of $\sim$5 kV cm^{-1}. The anti-crossing energy for $E_1 \leftrightarrow E_2$ is $\sim$5.9 meV. For the electrical fields between 6 and 15 kV cm^{-1}, E_1 resides in the lower quantum dot and E_2 resides in the upper quantum dot. The increase in the electric field up to $\sim$15 kV cm^{-1} results in a second anti-crossing $E_2 \leftrightarrow E_3$ between s-type upper quantum dot state (E_2) and p-type lower quantum dot state (E_3). The anti-crossing energy for this s–p anti-crossing ($\sim$0.7 meV) is much smaller than the previous s–s anti-crossing energy. This anti-crossing involves states that are higher in energy as measured from the relative bottom of the quantum well. The barrier height that separates/couples the states is noticeably smaller. As such the reduced coupling strength is at first unintuitive. The magnitude of the anti-crossing energy depends on the wavefunction overlap and the symmetries of the states involved [37]. The s–p anti-crossing energy will be smaller than the s–s anti-crossing energy because of the different spatial symmetries of the s- and p-states and smaller overlap between these two orbitals. Beyond $\vec{F} = 15$ kV cm^{-1}, both E_1 and E_2 are the atomic states confined in the lower quantum dot. Further electric-field-induced shift will bring E_4 (lower quantum dot state) into resonance with E_3 (upper quantum dot state) and exhibit a third anti-crossing $E_3 \leftrightarrow E_4$ between the s-type upper quantum dot state and the p-type lower quantum dot state. The anti-crossing energy for $E_3 \leftrightarrow E_4$ is $\sim$1.1 meV. Since the experiment [12] was performed for the electric field varying from 15 to 21 kV cm^{-1}, the experimentally observed anti-crossing (see figure 1(b)) is only $E_3 \leftrightarrow E_4$.

9. Spatial separation of electron and hole states by Stark shift analysis

The strength of the electric-field-induced shift in the lower quantum dot energies depends on the separation between the quantum dots as the center of the electrical field lever arm shift is fixed at H_1 in the upper quantum dot. The slope of this shift calculated from figure 3(a) is $\Delta E/\Delta\vec{F} \sim -1.33$ meV kV^{-1} cm. This predicts the spatial separation between H_1 and the lower quantum dot electron states to be around 13.3 nm. Since the wetting layer separation is 10 nm, the center-to-center distance between the quantum dots is 11.5 nm. The small difference of 13.3–11.5 = 1.8 nm between the predicted value and the center-to-center distance of the quantum dots is due to spatial separation between the electron and hole states in the quantum dot. The hole states tend to reside closer to the top of the quantum dot and the electron states tend to reside closer to the bottom of the quantum dot [33]. This is also consistent with the slope of the upper quantum dot electron energy shift which is around $\Delta E/\Delta\vec{F} \sim -0.167$ meV kV^{-1} cm. This corresponds to an intra-dot electron–hole spatial separation of 1.67 nm, close to the value of 1.8 nm mentioned above.

10. Quantum dot spacing by Stark shift analysis

The spectrum shown in figure 3(a) clearly shows the spectroscopic probing of the lower quantum dot electron states by the upper quantum dot state E_1. This technique is very useful to determine the geometry parameters of the molecular quantum dot. For example, if we do not know the separation between the quantum dots, the $E_1 \leftrightarrow E_2$ anti-crossing values of $\vec{\mathbf{F}}$ and the slope of the energy shifts can be used to estimate the separation between the quantum dots. In the quantum dot molecule under study, $E_4 - E_1$ is ∼19.9 meV as shown in figure 2(a) at $\vec{\mathbf{F}} = 0$. The anti-crossing between these two states occurs at ∼18.3 kV cm^{-1}. This gives approximately 10.87 nm separation between the two quantum dots which is very close to the value of ∼10 nm provided by the TEM measurements [12]. Thus the spacing between the anti-crossings and the electric-field-induced Stark shift allows us to 'reverse engineer' the separation between the quantum dots inside the quantum dot molecule.

11. Optically active states can be referred to as the upper quantum dot ground states

The ground hole state H_1 resides in the upper quantum dot as shown in figure 2 in this field direction regardless of the field strength. We therefore mark this state as the ground hole state of the upper quantum dot: $H_g \rightarrow U$. The electron ground state of the upper quantum dot is marked as $E_g \rightarrow U$ and shown as a horizontal dotted line in figure 3(a). The optically active exciton will always be comprised of these two ground states of the upper quantum dot. It should be pointed out that, although $E_g \rightarrow U$ is referred to as the upper quantum dot ground state, this energy state undergoes several anti-crossings with the lower quantum dot states and exhibits atomic and molecular characters at the increasing values of the electric fields. More importantly at the anti-crossing point $E_3 \leftrightarrow E_4$, the $E_g \rightarrow U$ state hybridizes with the lower quantum dot P-state. This is very critical because it determines the importance of the piezoelectric fields which has a stronger effect for electron p-states as compared to electron s-states as will be described in detail later.

12. Valence band spectroscopy—hole anti-crossings

Figure 3(a) also demonstrates the distribution of the hole energy level anti-crossings as a function of the applied electric field. The electric field pushes the hole energy levels of the lower quantum dot further to the lower energy values and thus provides a spectroscopic image of the upper quantum dot hole energy levels as they anti-cross between the two quantum dots. Since H_1 is in the upper quantum dot at $\vec{\mathbf{F}} = 0$, it remains in the upper quantum dot for the applied electric field direction and the valence band edge tilt. H_2 is in the lower quantum dot and, as it moves down, it couples with upper quantum dot states and gives rise to the anti-crossings $H_2 \leftrightarrow H_3$ and $H_3 \leftrightarrow H_4$. The hole anti-crossing energies are ∼0.2 meV and ∼0.1 meV for $H_2 \leftrightarrow H_3$ and $H_3 \leftrightarrow H_4$, respectively. These hole anti-crossing energies are significantly smaller than the corresponding electron anti-crossing energies, indicating a much stronger hole localization. Notably in the range of the experimental electric field from 15 to 21 kV cm^{-1}, all the four hole levels are in the upper quantum dot and no anti-crossing is observed. This implies that the electron states in the lower quantum dot exhibit weak optical transition strengths with the first four hole energy levels and hence are not measured experimentally.

13. Energy spectrum without and with piezoelectricity in the range of experiment

The comparison of figures 3(a) and (b) highlights the impact of the piezoelectric fields on the energy spectrum of the quantum dot molecule under study. The piezoelectricity insignificantly impacts the hole energy spectrum. The hole energy levels exhibit only a small energy shift. Only minor changes are observed in the hole anti-crossings. The electron ground state energies of the two quantum dots, namely E_1 and E_2, and their anti-crossing $E_1 \leftrightarrow E_2$ are also shifted by a small amount. However, the electron excited states (E_3, E_4) are significantly affected. Piezoelectricity increases the splitting between E_3 and E_4 and thus changes the position of the anti-crossing $E_2 \leftrightarrow E_3$ on the electric field axis. With piezoelectricity, $E_2 \leftrightarrow E_3$ occurs outside the range of experimentally applied electric field; without piezoelectricity, on the other hand, the anti-crossing $E_2 \leftrightarrow E_3$ is pushed inside the range of the experimentally applied electric field. This implies that, without the piezoelectric field, there will be two anti-crossings in the range of the electric field from 15 to 21 kV cm^{-1}, which contradicts the experimental measurements as shown in figure 1(b). The spectra for the electric fields between 15 and 21 kV cm^{-1} are enlarged in figures 3(c) and (d) to further explain the anti-crossings in this range of applied electric field.

Figures 3(c) and (d) depict the three exciton energies (E_2, H_1), (E_3, H_1) and (E_4, H_1) of the system with (c) and without (d) piezoelectric potential as a function of applied electric field. The H_1 hole as well as the E_2, E_3 and E_4 electron wavefunctions are depicted as the insets for a few critical fields. If both the electron and hole states are in the same quantum dot, the resulting exciton is called a 'direct exciton'. It corresponds to an optically active state due to large electron–hole overlaps. On the other hand, if the electron and hole states are in different quantum dots, then the exciton is called an 'indirect exciton'. It corresponds to an optically inactive state as the electron and hole overlap is negligible. Energy perturbations due to the quantum confined Stark effect (QCSE) in the direct and indirect excitons under applied bias exhibit different slopes: $\triangle E_{\text{exciton}} = p \cdot \vec{\mathbf{F}}$, where p is the dipole moment of the exciton and $\vec{\mathbf{F}}$ is the applied electric field. The exciton dipole moment is defined as: $p = q \cdot d$, where q is the electronic charge and d is the electron–hole spatial separation. For a direct exciton, the electron and hole both are in the same quantum dot, and are separated by a very small distance (typically $d \leqslant 1$ nm). The resulting magnitude of the Stark shift is therefore very small. For an indirect exciton, the electron and hole are in different quantum dots and separated by a large spatial distance ($d \geqslant 10$ nm in our case). In this case, the dipole moment

will be large and results in a strong magnitude of the Stark shift [33]. Figures 3(c) and (d) depict the direct and indirect natures of the excitons over the range of applied bias. As the figures indicate, a strong (larger slope) and a weak (smaller slope) Stark effect correspond to an indirect and direct exciton, respectively.

14. With piezoelectricity → one anti-crossing in the experimental data range

The experimentally measured optical spectra (circles and triangles in figures 3(e) and (f)) show the relative strengths of the two excitonic emissions 'A' and 'B'. At $\vec{\mathbf{F}} = 15$ kV cm^{-1}, the excitonic emissions 'A' is bright and 'B' is dark. As the electric field is increased, the intensity of 'A' becomes weaker and the intensity of 'B' gets stronger. The optical strengths of both excitons 'A' and 'B' become comparable at the electrical field value of 18.8 kV cm^{-1} where these two excitons anti-cross. For the higher values of the applied electrical field, the intensity of 'A' quenches rapidly and 'B' becomes optically bright. We compute the transition rate intensities using Fermi's golden rule as the squared absolute value of the momentum matrix: $|\langle \mathrm{E}_{2or3or4}|[\vec{n}, \mathbf{H}]|\mathrm{H}_1\rangle|^2$, where $\mathbf{H}$ is a single-particle tight binding Hamiltonian, $E_{2or3or4}$ are electron states, H_1 is the topmost valence band hole state and $\vec{n}$ is the position vector along the polarization direction of the incident light [32, 39–41]. Figure 3(e) compares the relative transition rate intensities $I_{(\mathrm{E}_4,\mathrm{H}_1)or\ (\mathrm{E}_3,\mathrm{H}_1)}/(I_{(\mathrm{E}_4,\mathrm{H}_1)} + I_{(\mathrm{E}_3,\mathrm{H}_1)})$, where $I_{(E_4,\mathrm{H}_1)}$ and $I_{(\mathrm{E}_3,\mathrm{H}_1)}$ are the transition rate intensities of $(\mathrm{E}_4, \mathrm{H}_1)$ and $(\mathrm{E}_3, \mathrm{H}_1)$, respectively, corresponding to figure 3(a) in the experimental field range. Figure 3(f) compares the relative transition rate intensities $I_{(\mathrm{E}_2,\mathrm{H}_1)}$or $I_{(E_3,\mathrm{H}_1)}$or $I_{(\mathrm{E}_4,\mathrm{H}_1)}/(I_{(\mathrm{E}_4,\mathrm{H}_1)} + I_{(\mathrm{E}_3,\mathrm{H}_1)} + I_{(\mathrm{E}_2,\mathrm{H}_1)})$, where $I_{(\mathrm{E}_2,\mathrm{H}_1)}$, $I_{(\mathrm{E}_3,\mathrm{H}_1)}$ and $I_{(\mathrm{E}_4,\mathrm{H}_1)}$ are the transition rate intensities of $(\mathrm{E}_2, \mathrm{H}_1)$, $(\mathrm{E}_3, \mathrm{H}_1)$ and $(\mathrm{E}_4, \mathrm{H}_1)$, respectively, corresponding to figure 3(b) in the experimental field range. Figure 3(e) compares the calculated optical strengths from the NEMO 3D simulator including the piezoelectric effects with the experimental measurements. In this case, as the electric field is increased, the intensity of $(\mathrm{E}_3, \mathrm{H}_1)$ reduces rapidly, whereas the intensity of $(\mathrm{E}_4, \mathrm{H}_1)$ increases. Figure 2(c) plots the excitonic energies $(\mathrm{E}_2, \mathrm{H}_1)$, $(\mathrm{E}_3, \mathrm{H}_1)$ and $(\mathrm{E}_4, \mathrm{H}_1)$ as a function of the applied electric field. Since E_2 remains in the lower quantum dot forming an indirect exciton with respect to H_1, $(\mathrm{E}_2, \mathrm{H}_1)$, in the range of the applied electric field from 15 to 21 kV cm^{-1}, its optical strength is very weak and is not measured in the experiment. The exciton $(\mathrm{E}_3, \mathrm{H}_1)$ is a direct exciton at 15 kV cm^{-1} and results in a strong optical peak. The increase in the electric field results in the tunneling of E_3 from the upper quantum dot to the lower quantum dot, which changes the character of $(\mathrm{E}_3, \mathrm{H}_1)$ from an optically active state to an optically inactive state at $\vec{\mathbf{F}} \sim 18.8$ kV cm^{-1}. In the vicinity of the anti-crossing point ($\vec{\mathbf{F}}$ from ∼17.9 to ∼20.5 kV cm^{-1}), two excitons $(\mathrm{E}_3, \mathrm{H}_1)$ and $(\mathrm{E}_4, \mathrm{H}_1)$ are tuned into resonance and exhibit close to equal magnitudes of intensity. In that field range, the electron states (E_3 and E_4) are found to be delocalized over two quantum dots showing a molecular-like nature rather than representing well-confined atomic states. Note that the relative intensities of the excitons in figure 3(e) calculated by our model closely follow the slopes of the experimental curves. NEMO 3D is hence able to correctly capture the dynamics of controlled coupling under the resonance of excitons. The controlled coupling of quantum dots under external bias (gate voltage) is critical in the implementation of exciton qubits and may foster efforts in quantum information processing based on quantum dots.

15. Without piezoelectricity → two anti-crossing

Figure 3(f) compares the experimentally measured transition strengths ('A' and 'B') with the calculated transition strengths (solid lines) from the NEMO 3D simulator without including the piezoelectric effects. The calculated transition strengths indicate three bright peaks and two anti-crossings. At $\vec{\mathbf{F}} = 15$ kV cm^{-1}, the exciton $(\mathrm{E}_2, \mathrm{H}_1)$ is bright and the excitons $(\mathrm{E}_3, \mathrm{H}_1)$ and $(\mathrm{E}_4, \mathrm{H}_1)$ are dark. As the electric field increases, first $(\mathrm{E}_2, \mathrm{H}_1)$ anti-cross with the exciton $(\mathrm{E}_3, \mathrm{H}_1)$. Further increase in the electric field results in another anti-crossing between the excitons $(\mathrm{E}_3, \mathrm{H}_1)$ and $(\mathrm{E}_4, \mathrm{H}_1)$. Figure 3(d) plots the corresponding excitonic energies as a function of the applied electric field ($\vec{\mathbf{F}}$). The direct and indirect nature of the excitons follow the optical transition strength patterns of figure 3(d). At $\vec{\mathbf{F}} = 15$ kV cm^{-1}, the exciton $(\mathrm{E}_2, \mathrm{H}_1)$ is direct and the excitons $(\mathrm{E}_3, \mathrm{H}_1)$ and $(\mathrm{E}_4, \mathrm{H}_1)$ are indirect excitons. The first anti-crossing makes the exciton $(\mathrm{E}_2, \mathrm{H}_1)$ indirect and the exciton $(\mathrm{E}_3, \mathrm{H}_1)$ direct. The second anti-crossing makes the exciton $(\mathrm{E}_3, \mathrm{H}_1)$ indirect and the exciton $(\mathrm{E}_4, \mathrm{H}_1)$ direct. In short, the excitonic spectra without piezoelectricity as shown in figures 3(d) and (f) result in three bright excitonic emissions, which disagree with the experimentally measured spectra.

Notably from figures 3(c) and (d), the anti-crossings of the electron states in the range of the experimental measurements involve electron p-states of the lower quantum dot. Since the piezoelectric effects are more pronounced in the excited states [23–26, 28, 29, 38], the correct identification of optically active states in the experimental measurements is of crucial importance. If the experimental emissions came from the ground state, the piezoelectric effects would be of minor importance and merely a small correction in the excitonic energies. Figures 3(c) and (d) clearly show that including piezoelectric effects is important to obtain the correct resonance at the point of anti-crossing. Furthermore the field dependence of the optical intensity is also different between the two cases of with piezo and without piezo. We obtain the smoothly varying intensity variation as obtained by the experiment only when the piezoelectric fields are included [12].

16. Piezoelectric model

Piezoelectricity is calculated from electric polarization originating from stressed crystals lacking inversion symmetry [29]. InGaAs/GaAs quantum dots are nanostructures with a lattice mismatch (∼7%) which leads to long-range strain fields penetrating deep into the surrounding buffer [22, 27, 38]. The diagonal and off-diagonal (shear) strain components can result in a built-in piezoelectric polarization, which cannot be

ignored. Bester *et al* [24] and Ahmed *et al* [27] outlined the importance of the linear piezoelectric effect for single InAs quantum dots. Later, Bester *et al* [25] highlighted the significance of the second-order (quadratic) component of piezoelectricity. They concluded that the second-order piezoelectric effect cancels the first-order (linear) component, thus leading to a net piezoelectric effect which was significantly suppressed. Following their argument that the net piezoelectric effect and its impact on the excitonic spectrum is negligible, they claimed that it is better not to consider piezoelectric effects at all rather than including only the linear component of the piezoelectric effect. On the other hand, Schliwa *et al* [28, 29] have indicated the importance of net piezoelectricity for some shapes and sizes of single quantum dots. The work presented here on quantum dot molecules clearly emphasizes that net piezoelectric effects cannot be neglected and are of critical importance in determining correct excitonic emission spectra in a coupled dot system that involves occupation of excited states.

In our model, the piezoelectric potential is included into the single-particle Hamiltonian according to the recipe of [24, 29]. First both linear $\mathbf{P}_1$ (first-order) and quadratic $\mathbf{P}_2$ (second-order) polarizations are separately calculated from the strain tensor components (equations (1) and (2)) using already published polarization constants (e_{14}, B_{114}, B_{124}, B_{156}) (see table 1) [24, 25]. They are then added to calculate the total polarization $\mathbf{P} = \mathbf{P}_1 + \mathbf{P}_2$:

$$\mathbf{P_1} = 2e_{14}\begin{pmatrix}\varepsilon_{yz}\\ \varepsilon_{xz}\\ \varepsilon_{xy}\end{pmatrix} \tag{1}$$

$$\mathbf{P_2} = B_{114}\begin{pmatrix}\varepsilon_{xx}\varepsilon_{yz}\\ \varepsilon_{yy}\varepsilon_{xz}\\ \varepsilon_{zz}\varepsilon_{xy}\end{pmatrix} + B_{124}\begin{pmatrix}\varepsilon_{yz}(\varepsilon_{yy}+\varepsilon_{zz})\\ \varepsilon_{xz}(\varepsilon_{zz}+\varepsilon_{xx})\\ \varepsilon_{xy}(\varepsilon_{xx}+\varepsilon_{yy})\end{pmatrix} \times B_{156}\begin{pmatrix}\varepsilon_{xz}\varepsilon_{xy}\\ \varepsilon_{yz}\varepsilon_{xy}\\ \varepsilon_{yz}\varepsilon_{xz}\end{pmatrix}. \tag{2}$$

The divergence of the total polarization $\mathbf{P}$ is calculated over a rectangular mesh using a finite difference approach to calculate total charge density $\boldsymbol{\rho}(\mathbf{r})$:

$$\boldsymbol{\rho}(\mathbf{r}) = -\nabla \cdot \mathbf{P}. \tag{3}$$

Finally, the Poisson equation (4) is solved to calculate the piezoelectric potential $V_{\mathrm{p}}(\mathbf{r})$, taking into account the position dependence of the static dielectric constant, $\varepsilon_{\mathrm{s}}(\mathbf{r})$. The value of the dielectric constant for vacuum ε_0 is 8.85×10^{-12} F m^{-1}. For InGaAs and GaAs materials, we used the relative dielectric constant values of $14.0\varepsilon_0$ and $12.84\varepsilon_0$, respectively:

$$\rho(\mathbf{r}) = \varepsilon_0 \nabla \cdot [\varepsilon_{\mathrm{s}}(\mathbf{r}) \nabla V_{\mathrm{p}}(\mathbf{r})]. \tag{4}$$

17. Quadrupole nature of the piezoelectric potentials

Figure 4(a) shows the first-order (solid line with squares), the second-order (dashed line) and the sum of the first-and second-order (solid line with circles) piezoelectric potentials along the [001] direction through the center of the quantum dot molecule. It is evident that the net piezoelectric potential is nonzero inside the quantum dot and penetrates into the surrounding GaAs buffer. The reason for a nonzero net potential inside the quantum dot is that the quadratic (second order → dashed line) component of the potential is significantly reduced for alloyed quantum dots ($In_{0.5}Ga_{0.5}As$) due to the following reasons. (1) Increasing the 'Ga' concentration reduces the diagonal strain components that determine the quadratic component. (2) The polarization constant B_{124}, which comprises a major portion of quadratic component, is reduced in magnitude. The linear (first order → solid line with square) component on the other hand increases mainly due to the large increase of e_{14}. The reduced quadratic component cannot cancel the effect of the already enhanced linear component, and hence the interior of the quantum dot, will have a nonzero potential largely dominated by the linear component (see the solid line with circle). Outside of the quantum dot, the quadratic component is negligible, and only the linear component is dominant. As a result, the net piezoelectric effect inside and at the interfaces of the quantum dots is no longer negligible.

Figures 4(b) and (c) show the net piezoelectric potential along the diagonal [110] and [$\bar{1}$10] directions through the center of the upper quantum dot. Figures 4(d) and (e) show the two-dimensional contour plots of the net piezoelectric potentials about 1 nm above the base of the lower and upper quantum dots. The quadrupole nature of the net piezoelectric potentials along the diagonal directions is clearly evident. The piezoelectric potentials along the [110] and [$\bar{1}$10] directions are large at the interfaces, where strain is large, and penetrate deep inside the GaAs buffer [26, 27]. A large GaAs buffer is therefore not only required along the [001] direction, but also in the plane of the quantum dot to fully capture the effect of the piezoelectric potential reaching 25–30 nm deep into the GaAs buffer. The wide extension of the piezoelectric fields in the lateral plane also implies that the quantum dots that are closer than ∼30 nm will interact with each other through the piezoelectric potentials.

Past studies [26–29] have shown that the quadrupole nature of the piezoelectric effect significantly changes the splitting and orientation of electron p-states which are already oriented along diagonal directions due to atomistic interface and strain asymmetry. In figure 1(b), the optically active states in the experimental spectrum are identified as excited states (E_3 and E_4) in the range of applied bias. Section 18 shows that considering piezoelectric effects is indeed critical in reproducing the experimental excitonic spectrum.

18. Quantitative explanation of 'one' versus 'two' anti-crossings

Figure 5 presents a quantitatively explanation of the presence of 'one' and 'two' anti-crossings. It shows a flow diagram in two directions: (flow to right) first six electron states without piezoelectricity and without electric field → with piezoelectricity but without electric field → with piezoelectricity and with 15 kV cm^{-1} electric field, (flow to left) first six electron states without piezoelectricity and

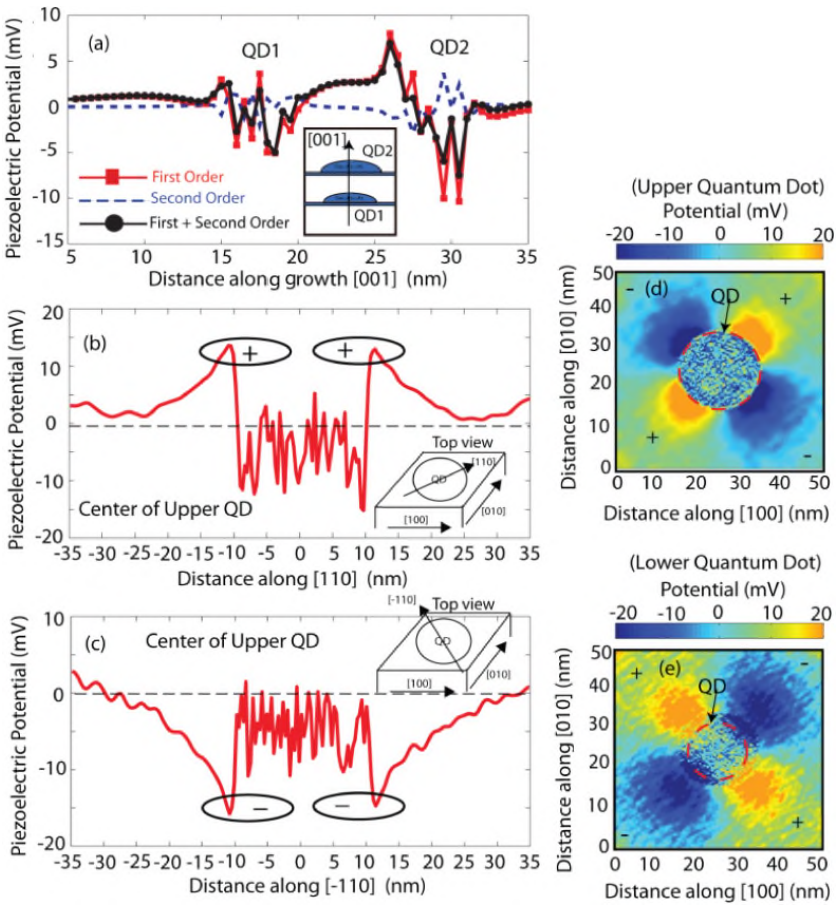

Figure 4. (a) The first-order (line with the box), second-order (dashed line) and the sum of first-and second-order (line with the circle) piezoelectric potential are shown through the center of the quantum dot along the [001] growth direction. The net potential is clearly nonzero inside the quantum dots and at the interfaces of the quantum dot and surrounding buffer. The second-order piezoelectric effect is weak and cannot cancel first-order effect inside the quantum dot. (b), (c) Piezoelectric potential plotted through the center of the upper quantum dot in the [110] and [$\bar{1}$10] directions. The origin of the x axis is taken at the center of the quantum dot. The quadrupole nature of the potentials is clearly evident: the potential is positive at the interface of the quantum dot and buffer along the [110] direction, whereas it is negative at the interface of quantum dot and buffer along the [$\bar{1}$10] direction. The random nature of potential inside the quantum dot region is a result of the random alloy configuration of $In_{0.5}Ga_{0.5}As$ quantum dot material. The quadrupole nature of the piezoelectric potential along diagonal directions strongly affects the splitting and orientation of electron p-states which are aligned along these directions because of atomistic asymmetry. (d), (e) The two-dimensional (xy) contour plots of the net piezoelectric potential at the base of the lower and upper quantum dots are shown as a function of distance along the [100] and [010] axis. The quadrupole nature of the potential is clearly evident from the plots. Also, the potential is long range and penetrates deep inside the GaAs buffer. This imposes the necessity of large GaAs buffer in the lateral dimensions to fully incorporate the effect of potential in the electronic structure calculations.

without electric field $\rightarrow$ without piezoelectricity and with 15 kV cm^{-1} electric field. It is critical to understand the arrangement of the electron states at 15 kV cm^{-1} because, at electric field values from 15 to 23 kV cm^{-1}, this will determine the resonance coupling. Since the first hole state remains in the upper quantum dot throughout the sweeping of the applied electrical field, it is not shown in figure 5. Piezoelectricity shifts the ground electron state $E_1(U-S)$ only by a very small value of 0.59 meV. The major contribution towards the shifting of the ground electron state comes from the externally applied bias. Hence the total shift in this state in either direction is approximately the same: left $= 15.09$ meV, right $= 15.01 + 0.59 = 15.6$ meV. The most significant effect of the piezoelectric effect is found to be on the $E_5(L-P_x)$ and $E_6(L-P_y)$ electron states. These states are not only shifted by a larger magnitude, but also their relative order is changed. Similar behavior has been observed in previous studies for a single quantum dot [25–27, 29], in which a strong piezoelectric effect has been shown to flip the order of the electron p-states. Here, the piezoelectric effect induces a shift of 0.7 meV and 3.2 meV in $E_5(L-P_x)$ and $E_6(L-P_y)$, respectively, followed by an additional electric-field-induced shift of 7.7 meV and 11.5 meV, respectively. This total shift of $3.2 + 11.5 = 14.7$ meV causes $E_6(L-P_y)$ to become $E_2(L-P_y)$ at 15 kV cm^{-1}, which is below $E_3(U-S)$ on the same energy scale. A further increase of the electric field beyond 15 kV cm^{-1} will shift $E_3(U-S)$ to higher energies and $E_4(L-P_x)$ to lower energies. This will result in resonant coupling of these two states with one anti-crossing ($E_3 \rightarrow E_4$) in the emission spectra. In the left direction

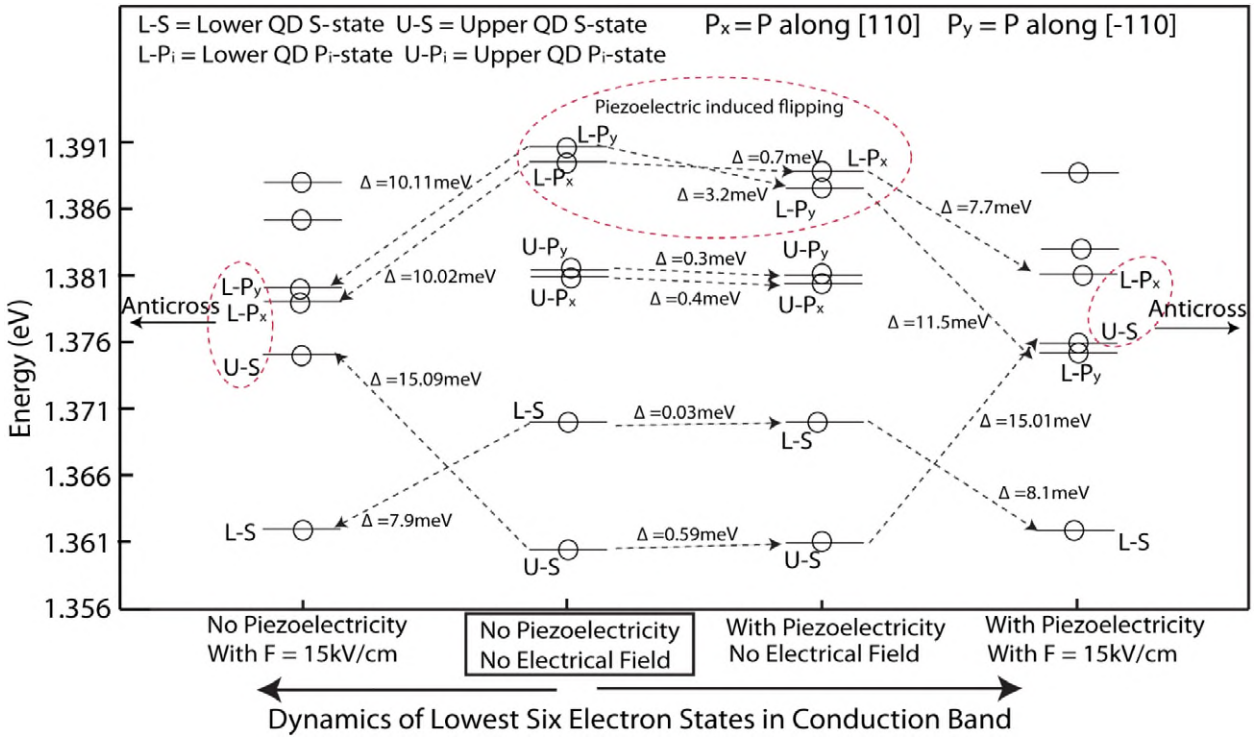

Figure 5. Flow diagram showing the ordering and position of first six electron states in the conduction band of quantum dot molecule. Starting from 'no piezoelectricity' case, the right direction shows the inclusion of piezoelectric effect and 15 kV cm^{-1} field effects. The left direction shows application of electric field directly after 'no piezoelectricity' case without including piezoelectric effect. Piezoelectric effect reorders p-states in the lower quantum dot and plays a critical role in determining the resonance at higher electrical field.

with no piezoelectricity included, there will be no additional shift of 3.2 and 0.7 meV in the lower quantum dot p-states. Mere electric-field-induced shifts of 10.02 and 10.11 meV are not sufficient enough to push either of the two excited states below $E_2(U-S)$. This will result in two anti-crossings ($E_2 \rightarrow E_3 \rightarrow E_4$).

19. Conclusions

In conclusion, a detailed systematic atomistic tight binding study of the experimental single-quantum-dot molecular geometry is presented, taking into account the long-range strain, the atomistic interface asymmetry, and both the linear and the quadratic piezoelectric effects. The quantum dot molecular energy states are composed of individual single quantum dot states which can interact with each other depending on their energetic alignment. The external electric field enables the tuning of the relative alignment of molecular and atomic states which has been observed in experimental spectroscopy data [12]. Our calculations quantitatively reproduce the experimental spectra. The interband transition strengths are calculated to compare the relative intensities of the excitonic emissions and characterize them as optically active and inactive states. The calculated transition strengths closely follow the experimentally measured intensities and identify the excited electron (p-states) states as the optically active states in the range of the applied electrical field. The close quantitative agreement of our theoretical calculations with the experimental data [12] allows us to gain significant physical insight of a quantum dot molecule. We sweep the electric field from 0 to 21 kV cm^{-1} and provide a spectroscopic mapping of the lower quantum dot electron states and the upper quantum dot hole excited states. Analysis of the observed sequence of the anti-crossings provides a technique to precisely probe the energy states of one quantum dot with the help of the energy states of the neighboring quantum dot. The direction of the applied electrical field determines the quantum dot whose electron/hole electronic states will be probed by increasing the electrical field magnitude. This technique can be used to 'reverse engineer' the geometry of the quantum dot molecule from the experimentally measured optical spectrum.

The strain and piezoelectric fields are both found to be long-range effects. This imposes the need of a large size of simulation domain consisting of about 15 million atoms in the strain domain and about 9 million atoms in the electronic domain. Our calculations include both the first-order and the second-order piezoelectric fields. The quadrupole nature of the net piezoelectric effect along the [110] and [$\bar{1}$10] directions significantly affects the splitting and orientation of the excited electron states. The NEMO 3D-based atomistic study shows that the net piezoelectric effect is critical in reproducing the experimentally observed optical transitions that are dominated by excited states such as devices tuned with electric fields. Continuum methods such as the effective mass model and the $k \cdot p$ method do not take into account the atomistic nature of the InGaAs quantum dots and thus cannot correctly incorporate

the strain and piezoelectric fields. The quantitative modeling of the experimental spectra [12] presented here allows us to extend our model for charged excitonic calculations. We are implementing the calculations of charged excitons in our model and a detailed analysis of a complex excitonic spectrum such as measured in [37] will be presented in future.

Acknowledgments

MU acknowledges the Fulbright fellowship funding from the USA Department of State (grant ID no. 15054783). https://nanoHUB.org computational resources operated by the Network for Computational Nanotechnology (NCN) and funded by the National Science Foundation (NSF) are used for this work. MT acknowledges funding by the German Academic Exchange Service (DAAD) and a fellowship by the German National Merit Foundation (Studienstiftung des Deutschen Volkes). GK and HR acknowledge funding by the National Science Foundation (NSF). SA would like to acknowledge the ORNL/ORAU HPC Grant 2009. HK acknowledges support from DFG via the Emmy Noether Program and Nanosystem Initiative Munich (NIM).

References

[1] Michler P 2003 *Single Quantum Dot* (Berlin: Springer)
[2] Bimberg D 2008 *Semiconductor Nanostructures* (Berlin: Springer)
Bimberg D, Grundmann M and Ledentsov N N 1999 *Quantum Dot Heterostructures* (Chichester: Wiley)
[3] Bondeo N H, Erland J, Gammon D, Park D, Katzer D S and Steel D G 1998 *Science* **282** 1473
[4] Li X *et al* 2003 *Science* **301** 809
[5] Loss D and DiVincenzo D P 1998 *Phys. Rev.* A **57** 120
[6] van der Wiel W G, Franceschi S D, Elzerman J M, Fujisawa T, Tarucha S and Kouwenhoven L P 2003 *Rev. Mod. Phys.* **75** 1
[7] Gywat O, Burkard G and Loss D 2002 *Superlatt. Microstruct.* **31** 127
[8] Li X Q and Arakawa Y 2000 *Phys. Rev.* A **63** 012302
[9] Lovett B W, Reina J H, Nazir A and Briggs G A 2003 *Phys. Rev.* B **68** 205319
[10] Oosterkamp T H *et al* 1998 *Nature* **395** 873
[11] Bayer M *et al* 2001 *Science* **291** 451
[12] Krenner H J, Sabathil M, Clark E C, Kress A, Schuh D, Bichler M, Abstrieter G and Finely J J 2005 Direct observation of controlled coupling in an individual quantum dot molecule *Phys. Rev. Lett.* **94** 057402
[13] Klimeck G *et al* 2007 Atomistic simulation of realistically sized Nanodevices using NEMO 3D: part I—models and benchmarks *IEEE Trans. Electron Devices* **54** 2079–89
[14] Klimeck G, Ahmed S, Kharche N, Korkusinski M, Usman M, Prada M and Boykin T B 2007 Atomistic simulation of realistically sized nanodevices using NEMO 3D: part II—applications *IEEE Trans. Electron Devices* **54** 2079–89
[15] Klimeck G, Oyafuso F, Boykin T B, Bowen R C and Allmen P V 2002 Development of a nanoelectronic 3D (NEMO 3-D) simulator for multimillion atom simulations and its application to alloyed quantum dots *Comput. Model. Eng. Sci.* **3** 601–42
[16] Usman M, Ryu H, Woo I, Ebert D S and Klimeck G 2009 Moving towards Nano-TCAD through multi-million atom quantum dot simulations matching experimental data *IEEE Trans. Nanotechnol.* **8** 330
[17] Boykin T B, Klimeck G, Bowen R C and Oyafuso F 2002 Diagonal parameter shifts due to nearest-neighbor displacements in empirical tight binding theory *Phys. Rev.* B **66** 125207
[18] Keating P 1966 Effect of invariance requirements on the elastic strain energy of crystal with application to diamond structure *Phys. Rev.* **145** 737
[19] Rahman R, Wellard C J, Bradbury F R, Prada M, Cole J H, Klimeck G and Hollenberg L C L 2007 High precision quantum control of single donor spins in Si *Phys. Rev. Lett.* **99** 036403
[20] Lansbergen G P *et al* 2008 Gate induced quantum confinement transition of a single dopant atom in a Si FinFET *Nature Phys.* **4** 656
[21] Kharche N, Prada M, Boykin T B and Klimeck G 2007 Valley-splitting in strained silicon quantum wells modeled with 2° miscut, step disorder and alloy disorder *Appl. Phys. Lett.* **90** 092109
[22] Usman M, Ahmed S and Klimeck G 2008 Atomistic tight binding study of strain-reduced confinement potentials in identical and non-identical InAs/GaAs vertically stacked quantum dots *Proc. of 8th IEEE NANO (Arlington, TX, Aug. 2008)* pp 541–4
[23] Bester G, Wu X, Vanderbilt D and Zunger A 2006 Importance of second-order piezoelectric effects in zinc-blende semiconductors *Phys. Rev. Lett.* **96** 187602
[24] Bester G, Zunger A, Wu X and Vanderbilt D 2006 Effects of linear and nonlinear piezoelectricity on the electronic properties of InAs/GaAs quantum dots *Phys. Rev.* B **74** 081305(R)
[25] Bester G and Zunger A 2005 Cylindrically shaped zinc-blende semiconductor quantum dots do not have cylindrical symmetry: atomistic symmetry, atomic relaxation, and piezoelectric effects *Phys. Rev.* B **71** 045318
[26] Sundaresan S, Islam S and Ahmed S 2010 Built-in electric fields in InAs/GaAs quantum dots: geometry dependence and effects on the electronic structure *NMDC: Technical Proc. IEEE Nanotechnology Materials and Devices Conf. (California, Oct. 2010)* pp 30–5
[27] Ahmed S, Usman M, Kharche N, Schliwa A and Klimeck G 2007 Atomistic simulation of non-degeneracy and optical polarization anisotropy in pyramidal quantum dots *Proc. of IEEE NEMs (Bangkok, Jan. 2007)* pp 937–42
[28] Schliwa A, Winkelnkemper M and Bimberg D 2009 Few-particle energies versus geometry and composition of InGaAs/GaAs self-organized quantum dots *Phys. Rev.* B **79** 075443
[29] Schliwa A, Winkelnkemper M and Bimberg D 2007 Impact of size, shape, and composition on piezoelectric effects and electronic properties of In(Ga)As/GaAs quantum dots *Phys. Rev.* B **76** 205324
[30] Fonseca L R C, Jimenez J L and Leburton J P 1998 Electronic coupling in InAs/GaAs self-assembled stacked double-quantum-dot systems *Phys. Rev.* B **58** 9955
[31] Lazarenkova O L, von Allmen P, Oyafuso F, Lee S and Klimeck G 2004 Effect of anharmonicity of the strain energy on band offsets in semiconductor nanostructures *Appl. Phys. Lett.* **85** 4193
[32] Usman M, Ryu H, Lee S, Matthias Tan Y H and Klimeck G 2009 Quantum confined stark shift and ground state optical transition rate in [100] laterally biased InAs/GaAs quantum dots *IWCE: IEEE Proc.of 13th Int. Workshop on Computational Electronics (China May, 2009)*
[33] Fry P W *et al* 2000 *Phys. Rev. Lett.* **84** 733
[34] Doty M F, Climente J I, Greilich A, Yakes M, Bracher A S and Gommon D 2010 Hole spin mixing in InAs quantum dot molecule *Phys. Rev.* B **81** 035308
[35] Litvinov D *et al* 2008 Influence of InGaAs cap layers with different In concentration on the properties of InGaAs quantum dots *J. Appl. Phys.* **103** 083532

[36] Korkusinski M and Klimeck G 2006 Atomistic simulations of long-range strain and spatial asymmetry molecular states of seven quantum dots *J. Phys.: Conf. Ser.* **38** 75–8
[37] Scheibner M, Yakes M, Bracker A S, Ponomarev I V, Doty M F, Hellberg C S, Whitman L J, Reinecke T L and Gammon D 2008 Optically mapping the electronic structure of coupled quantum dots *Nature Phys.* **4** 291–5
[38] Ahmed S *et al* 2008 *Multimillion Atom Simulations with NEMO 3-D* (*Springer Encyclopedia for Complexity*) (Berlin: Springer) arXiv:(0901.1890v1)
[39] Boykin T B and Vogl P 2001 Dielectric response of molecules in empirical tight binding theory *Phys. Rev.* B **65** 035202
[40] Boykin T B, Bowen R C and Klimeck G 2001 Electromagnetic coupling and gauge invariance in the empirical tight binding theory *Phys. Rev.* B **63** 245314
[41] Graf M and Vogl P 1995 *Phys. Rev.* B **51** 4940
[42] Krenner H, private communication
[43] Bester G *et al* 2004 *Phys. Rev. Lett.* **93** 047401
Bester G *et al* 2005 *Phys. Rev.* B **71** 075325
[44] Usman M *et al* 2011 *J. Appl. Phys.* **109** 104510